Letter

Distorted 3*Q* state driven by topological-chiral magnetic interactions

Soumyajyoti Haldar,[1,*,†] Sebastian Meyer,[1,*,‡] André Kubetzka,[2] and Stefan Heinze[1]
[1]*Institute of Theoretical Physics and Astrophysics, University of Kiel, Leibnizstrasse 15, 24098 Kiel, Germany*
[2]*Department of Physics, University of Hamburg, 20355 Hamburg, Germany*

(Received 26 May 2021; revised 20 August 2021; accepted 21 October 2021; published 11 November 2021)

We predict the occurrence of unexpected magnetic ground states in ultrathin Mn films due to the frustration of higher-order interactions. Based on density functional theory we show that significant chiral-chiral interactions occur in hexagonal Mn monolayers due to large topological orbital moments which interact with the emergent magnetic field. Due to the competition with biquadratic and four-spin interactions superposition states of spin spirals such as the 2*Q* state or a distorted 3*Q* state arise. Simulations of spin-polarized scanning tunneling microscopy images suggest that the distorted 3*Q* state could be the magnetic ground state of a Mn monolayer on Re(0001).

DOI: 10.1103/PhysRevB.104.L180404

Noncollinear spin structures are of fundamental interest in magnetism since they allow to obtain insight into the underlying microscopic interactions and are promising for spintronic applications [1,2]. For example, the frustration of Heisenberg exchange interactions is the origin of spin spiral states found in many rare-earth elements or in the fcc phase of Fe. The competition with beyond nearest-neighbor exchange occurs due to the long-range nature of the Ruderman-Kittel-Kasuya-Yosida interaction characteristic for transition and rare-earth metals. Spin spirals can also arise due to the Dzyaloshinskii-Moriya (DM) interaction which is present in materials with broken inversion symmetry such as surfaces or interfaces [3].

Recently, more complex magnetic states such as the superposition of spin spirals [4–6] or atomic scale spin lattices [7–9] have raised much attention. They can occur due to terms beyond the pair-wise Heisenberg or DM interactions such as higher-order exchange interactions [10–12]. They might also be driven by the recently proposed topological-chiral [13] and chiral multispin interactions [14–16]. A prominent example of a multi-*Q* state—a superposition of symmetry equivalent spin spirals (1*Q* states)—is the 3*Q* state [4]. The 3*Q* state, which has been predicted as the ground state of a Mn monolayer on Cu(111) [4], is an intriguing noncollinear spin structure on a two-dimensional lattice which leads to topological orbital moments and a topological Hall effect even in the absence of spin-orbit coupling [17]. It has also been predicted to trigger topological superconductivity in a conventional superconductor [18]. Recently, the 3*Q* state has been discovered in a Mn monolayer on the Re(0001) surface by spin-polarized scanning tunneling microscopy (SP-STM) [6]. However, the locking of the spin structure to the atomic lattice could not be explained and it was speculated that a distortion of the 3Q state could be the origin.

Here we demonstrate based on density functional theory (DFT) that the frustration of higher-order interactions in ultrathin films leads to unexpected magnetic ground states. Besides fourth-order terms such as the biquadratic or four-spin interactions, which are typically considered, the chiral-chiral interaction which is of sixth order can play an essential role. For free-standing Mn monolayers we show that large topological orbital moments occur which interact with the emerging magnetic field leading to significant chiral-chiral interactions. By the interplay of this term with biquadratic and four-spin interactions, complex spin structures such as the 2*Q* state or the distorted 3*Q* state can be stabilized. For Mn monolayers on Cu(111) and Re(0001) we predict similarly large chiral-chiral interactions which can induce a distorted 3*Q* magnetic ground state for Mn/Re(0001). Simulated scanning tunneling microscopy images show that the predicted distorted 3*Q* ground state of Mn/Re(0001) is consistent with previous experiments.

We have used DFT as implemented in the FLEUR code [19] which is based on the full-potential linearized augmented plane wave method [20] to calculate total energies of noncollinear spin structures [21] for unsupported Mn monolayers and on the Re(0001) surface. We have also used the VASP code [22], which is based on the projector augmented wave method [23–25], to study Mn/Re(0001) and Mn/Cu(111). Calculations have been performed in the local density and scalar-relativistic approximation, i.e., neglecting spin-orbit coupling. Computational details can be found in the Supplemental Material [26].

For unsupported Mn monolayers we have calculated the energy dispersion of spin spirals since they are the fundamental solution of the classical Heisenberg model. Spin spirals can be characterized by a vector **q** from the Brillouin zone (BZ). The calculated energy dispersion is qualitatively the same for all considered Mn monolayers (see Ref. [26]). Among all spin spiral states, the row-wise antiferromagnetic (RW-AFM) state

*These authors contributed equally to this work.
†haldar@physik.uni-kiel.de, haldar.physics@gmail.com
‡Present address: Nanomat/Q-mat/CESAM, Université de Liège, B-4000 Sart Tilman, Belgium.

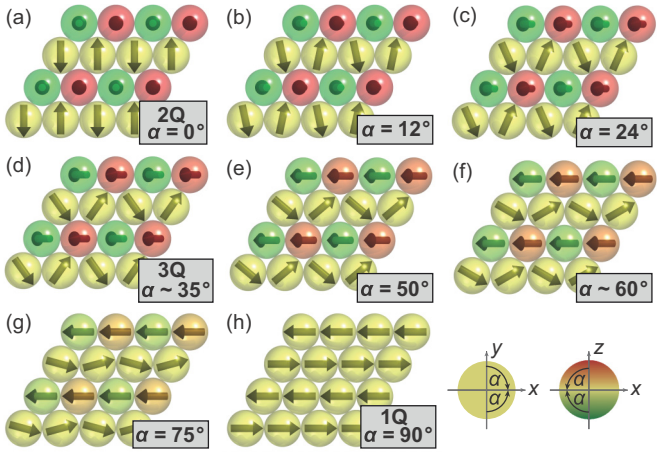

FIG. 1. Spin structures for a hexagonal Mn monolayer along the continuous path given by Eq. (1) from (a) the $2Q$ state via (d) the $3Q$ to (h) the $1Q$ state. Yellow arrows denote magnetic moments which rotate in the xy plane (shown in the coordinate system above), red arrows denote moments in the positive z direction, green arrows in the negative z direction. The angle α is applied to rotate $\pm z$ spins into the $-x$ direction and $\pm y$ spins to the $+x$ direction. (a) $2Q$ state with $\alpha = 0°$, (b) $\alpha = 12°$, (c) $\alpha = 24°$, (d) $3Q$ state with $\alpha \sim 35°$, (e) $\alpha = 50°$, (f) $\alpha \sim 60°$, (g) $\alpha = 75°$, (h) $1Q$ state (RW-AFM) with $\alpha = 90°$.

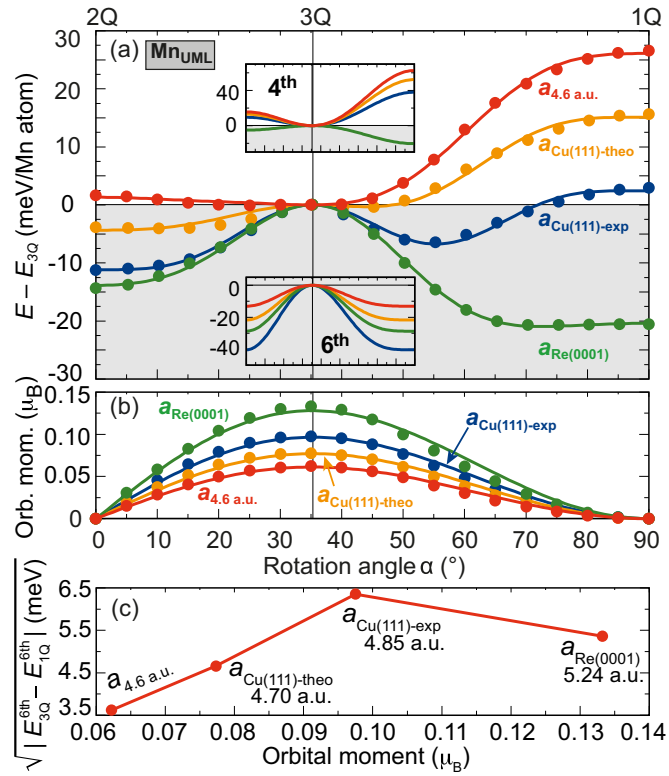

FIG. 2. (a) Energy along the $2Q$-$3Q$-$1Q$ path given by Eq. (1) in hexagonal Mn unsupported monolayers (UMLs) for different in-plane lattice constants. Symbols denote total energies calculated from DFT using the FLEUR code, the lines show the fit to higher-order exchange interaction terms. The two insets show the contribution of the fourth and sixth order terms to the fit. Red color shows the result for $a = 4.6$ a.u., orange and blue color for the theoretical and experimental in-plane lattice constant of Cu(111), respectively, and green color the values for the theoretical in-plane lattice constant of Re(0001) [27]. (b) Absolute value of the orbital moment per Mn atom along the direction perpendicular to the Mn UML. Symbols denote DFT values and lines the fit to the scalar spin chirality (see text for details). (c) Orbital moment of the $3Q$ state vs the absolute value of the sixth-order energy contributions at the $1Q$ with respect to the $3Q$ state [cf. lower inset of (a)].

[Fig. 1(h)] is the energetically lowest state and the exchange coupling is strongly antiferromagnetic. The RW-AFM state can propagate along one of the three symmetry equivalent directions of the surface corresponding to the $\overline{\mathrm{M}}$ points of the two-dimensional BZ, i.e., $1Q$ states. One can construct linear combinations of two or three of these degenerate $1Q$ states under the constraint of fixed spin length at every lattice site resulting in the $2Q$ [Fig. 1(a)] and the $3Q$ [Fig. 1(d)] state, respectively. These states are energetically degenerate with the $1Q$ states within the classical Heisenberg model. The established approach to determine the higher-order exchange constants in fourth order relies on DFT total energies of such multi-Q states [12].

In this work, we propose a path in the magnetic configuration space (Fig. 1) which allows us to go beyond fourth order terms and reveals different ground states. It is motivated by the speculation of a distorted $3Q$ ground state of Mn/Re(0001) [6]. We start from the $2Q$ state, Fig. 1(a), and rotate all spins in this structure continuously into the $1Q$ (RW-AFM) state, Fig. 1(h). This is achieved based on the Rodriguez rotation formula such that the spin $\mathbf{s}_i^\nu$ at site i in the νth rotation step is given by (see Ref. [26] for details)

$$\mathbf{s}_i^\nu = \mathbf{s}_i^{2Q} \cos\alpha_\nu + \mathbf{s}_i^{1Q} \sin\alpha_\nu, \tag{1}$$

where $\mathbf{s}_i^{2Q}$ and $\mathbf{s}_i^{1Q}$ are the spin directions in the $2Q$ and $1Q$ state, respectively. The rotation angle α_ν is varied from 0 to 90°. The $3Q$ state corresponds to $\alpha_\nu \approx 35°$, Fig. 1(d). It can be demonstrated that pair-wise Heisenberg exchange terms, $-J_{ij}(\mathbf{s}_i \cdot \mathbf{s}_j)$, where J_{ij} are the exchange constants, do not vary along this path (Ref. [26]). Therefore, any change of the total energy obtained via DFT can only be explained by terms beyond the Heisenberg exchange.

Figure 2(a) shows the total DFT energies calculated for the path defined by Eq. (1) via the FLEUR code for a hexagonal unsupported monolayer (UML) of Mn with different in-plane lattice constants, i.e., distance between nearest-neighbor atoms. For the Mn UML with a lattice constant of $a = 4.6$ a.u., we find that the $3Q$ state is the energetically lowest spin configuration. If we slightly increase the lattice constant to the value of the theoretical Cu lattice constant, the $2Q$ state shifts below the $3Q$ state. In addition, a small local energy minimum occurs close to the $3Q$ state. If the lattice constant is increased further to the experimental value of Cu, the energy minimum of the distorted $3Q$ state [Fig. 1(f)] becomes more pronounced but the $2Q$ state remains the lowest state. For the even larger Re lattice constant, the energy of the $1Q$ state has moved below the $2Q$ state. There is a tiny energy minimum for a distorted $1Q$ state with an angle of $\alpha \approx 75°$ [Fig. 1(g)].

The higher-order exchange interactions (HOIs) of fourth order are the biquadratic interaction and the three-site and four-site four spin interactions [12]:

$$\begin{aligned} H_{4\text{th}} = &-\sum_{i,j} B_{ij}(\mathbf{s}_i \cdot \mathbf{s}_j)^2 - \sum_{ijk} Y_{ijk}[(\mathbf{s}_i \cdot \mathbf{s}_j)(\mathbf{s}_j \cdot \mathbf{s}_k) \\ &+ (\mathbf{s}_j \cdot \mathbf{s}_i)(\mathbf{s}_i \cdot \mathbf{s}_k) + (\mathbf{s}_i \cdot \mathbf{s}_k)(\mathbf{s}_k \cdot \mathbf{s}_j)] \\ &- \sum_{ijkl} K_{ijkl}[(\mathbf{s}_i \cdot \mathbf{s}_j)(\mathbf{s}_k \cdot \mathbf{s}_l) + (\mathbf{s}_i \cdot \mathbf{s}_l)(\mathbf{s}_j \cdot \mathbf{s}_k) \\ &- (\mathbf{s}_i \cdot \mathbf{s}_k)(\mathbf{s}_j \cdot \mathbf{s}_l)], \end{aligned} \tag{2}$$

where B_{ij}, Y_{ijk}, and K_{ijkl} are the higher-order exchange constants which can be obtained via DFT [6,12,28].

The energy of these three terms varies along the given path according to the function $E_{4\text{th}}(\alpha) = \kappa_{4\text{th}}(2\cos^4\alpha + 6\sin^4\alpha - 4\cos^2\alpha\sin^2\alpha)$ with a strength $\kappa_{4\text{th}}$ (see Ref. [26]). This function has local extrema at the 1Q, 2Q, and 3Q state [see upper inset of Fig. 2(a)]. Since the 2Q state is always in between the 1Q and the 3Q state, i.e., it cannot be the lowest state as long as higher-order terms are restricted to fourth order, it has been excluded in previous DFT calculations for Mn UMLs and Mn/Cu(111) [4]. However, the total energy calculations for Mn UML [Fig. 2(a)] cannot be explained based on the higher-order interactions given by Eq. (2). Note that the DFT calculations were performed in the scalar-relativistic approximation, i.e., neglecting spin-orbit coupling, such that chiral-multispin interactions [14–16] cannot occur.

Recently, it has been demonstrated that, due to the interaction of the topological orbital moment, which can arise in noncollinear spin structures even in the absence of spin-orbit coupling [8,17], with the emergent magnetic field the so-called chiral-chiral interaction occurs [13,29]:

$$H_{\text{CC}} = -\sum_{ijk} \kappa^{\text{CC}}_{ijk}[\mathbf{s}_i \cdot (\mathbf{s}_j \times \mathbf{s}_k)]^2 \tag{3}$$

with a site-dependent interaction strength κ^{CC}_{ijk}. This sixth order interaction scales with the square of the scalar spin chirality $\chi_{ijk} = \mathbf{s}_i \cdot (\mathbf{s}_j \times \mathbf{s}_k)$ which varies for the given path at every site as $\chi_{ijk} \propto \cos^2\alpha\sin\alpha$ (see Ref. [26]). Therefore, the chiral-chiral interaction is proportional to $\cos^4\alpha\sin^2\alpha$ [lower inset of Fig. 2(a)].

In order to check the importance of this interaction in our Mn UMLs we have calculated via DFT the topological orbital moment, which is proportional to the scalar spin chirality [Fig. 2(b)]. As expected it exhibits a maximum at the 3Q state and vanishing values for the 2Q and 1Q state and is oriented perpendicular to the film. The orbital moment for the 3Q state is in good agreement with previous calculations [17]. An excellent fit is achieved for the angle dependent variation of the orbital moment [Fig. 2(b)] by using the analytical form of the scalar spin chirality given above.

The competition of fourth- and sixth-order interactions can explain the observed trend of the DFT energy curves for the Mn UMLs as shown by the insets of Fig. 2(a). The fourth-order contribution favors the 3Q state for the three smaller lattice constants and the 1Q state for the Re lattice constant. The sixth-order interaction, on the other hand, favors the 1Q and the 2Q state and drives the transition to the distorted 3Q state.

The trend of DFT curves in Fig. 2(a) is captured by considering only the fourth- and sixth-order (see Ref. [26]). To improve the fit, we added contributions from eighth- and tenth-order terms in Fig. 2(a). The need to go beyond fourth-order terms to fit DFT total energy curves has been noticed before but was not explained [30]. Such an expansion of a spin model for itinerant magnets in a power series of cosines between spins has been proposed in Ref. [31] starting from the Liechtenstein formula [32].

To show the significance of the chiral-chiral interaction, we take a closer look at the sixth-order term [lower inset of Fig. 2(a)]. The energy difference between the 3Q and the 1Q state of the sixth-order term increases proportional to the square of the topological orbital moment from $a = 4.6$ a.u. up to $a = 4.85$ a.u. [Fig. 2(c)]. This is expected since the chiral-chiral interaction is proportional to the square of the scalar spin chirality while the orbital moment is linear with this quantity. At the Re lattice constant, $a = 5.24$ a.u., the orbital moment further increases, while the energy contribution from the sixth order term decreases. Due to the large increase of the lattice constant the local density of states changes significantly (see Ref. [26]) and thereby also κ^{CC}_{ijk}, which depends on the electronic structure (cf. Supplementary Information of Ref. [13]).

Note, that the bicubic interaction $(\mathbf{s}_i \cdot \mathbf{s}_j)^3$, which is possible in systems with a spin moment of $\geqslant 3\mu_B$ [12], could also contribute to the sixth order energy term since it exhibits the same functional form along the given path (see Ref. [26]). However, the large topological orbital moments and the scaling of the sixth-order energy with the orbital moment provide strong evidence that the chiral-chiral interaction is dominating.

Now we turn to Mn monolayers on surfaces. The 3Q state has been predicted for Mn/Cu(111) [4], however, the 2Q state was not considered in that study. The DFT total energy curve along the path of Eq. (1) [Fig. 3(a)], obtained via VASP, is consistent with the expectation of Ref. [4], i.e., the 3Q state is lowest and the 2Q state lies between the 3Q and the 1Q states. However, a fit to the DFT data points can be significantly improved by taking a sixth order exchange term into account, in addition to the fourth order term [inset of Fig. 3(a)]. The topological orbital moments are of the same order of magnitude as for the UMLs and can be fit by the scalar spin chirality [Fig. 3(c)]. This shows that the chiral-chiral interaction is significant in this system.

Experimentally, the 3Q state was discovered in hcp-Mn/Re(0001) [6]. From previous DFT calculations it is known that the RW-AFM state (1Q state) is energetically lowest among all spin spiral states [6]. The 3Q state formed from a superposition of the three equivalent RW-AFM states [4] is even slightly lower in total energy. Surprisingly, the perfect 3Q state is only a local energy maximum along the path given by Eq. (1) while there are two local energy minima: one at the 2Q state and one for a distorted 3Q state [Fig. 3(b)]. In the FLEUR calculation the 2Q state is slightly lower in energy and in VASP the two states are energetically nearly degenerate [33].

Similar to the case of the UMLs, higher-order terms can significantly improve the fit of the energy curve of hcp-Mn/Re(0001) [inset of Fig. 3(b)]. In particular, the sixth order terms, corresponding to the chiral-chiral or bicubic

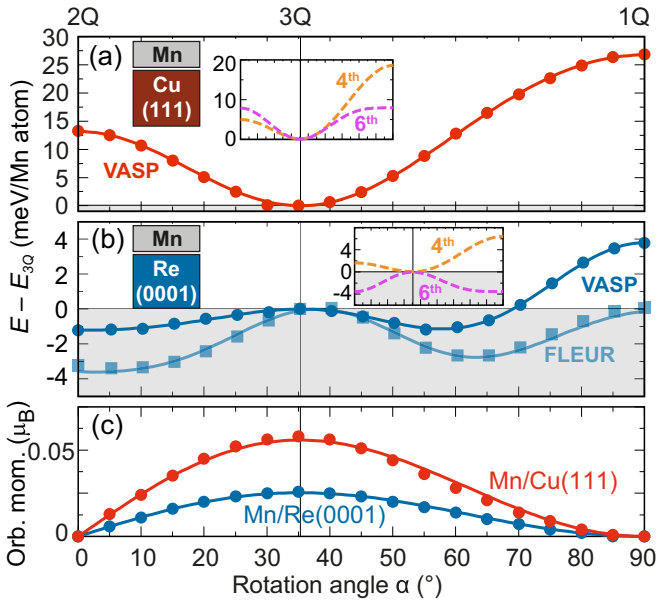

FIG. 3. Energy along the continuous $2Q$-$3Q$-$1Q$ path given by Eq. (1) for (a) Mn/Cu(111) and (b) hcp-Mn/Re(0001). Filled circles are energies calculated from DFT, the lines show the fit to higher-order-exchange interaction (insets show fourth and sixth order terms). For Mn/Cu(111) DFT calculations were performed using the VASP code and for hcp-Mn/Re(0001) both the FLEUR (squares) and the VASP codes (circles) were applied. (c) Absolute value of the orbital moment per Mn atom directed perpendicular to the surface. Symbols denote DFT values and lines the fit to the scalar spin chirality.

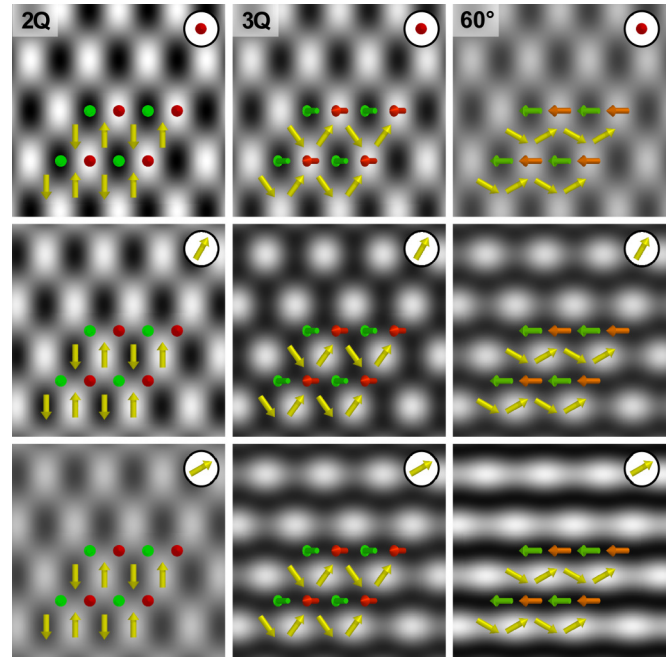

FIG. 4. Simulated spin-polarized scanning tunneling microscopy images at constant height (0.8 nm) for the $2Q$, the $3Q$, and the distorted $3Q$ (60°) state (left, middle, and right row, respectively) for three different tip magnetization directions as indicated in the upper right corner of every image. The simulations have been performed using the model described in Ref. [34]. All panels have the same color scale of 1.5 pm from black to white.

interaction, are decisive to capture the two local energy minima. The topological orbital moments are smaller for hcp-Mn/Re(0001) [Fig. 3(c)] than for Mn/Cu(111) and so is the sixth order energy contribution.

Complex noncollinear spin structures in ultrathin films as proposed in this work can be resolved down to the atomic scale using SP-STM [34–36]. In order to check whether the three magnetic states compared above can be distinguished in an experiment, we have simulated SP-STM images for the $2Q$ state, the $3Q$ state, and the distorted $3Q$ state for three different magnetization directions of the STM tip (Fig. 4). For the $2Q$ state the contrast is very similar for the three cases which indicates that different rotational domains will look the same. For the $3Q$ state, in contrast, the SP-STM image for an out-of-plane magnetized tip (middle panel in the upper row of Fig. 4) is qualitatively different from that for a tip with an in-plane magnetization component (lower two panels in the middle row). Thereby, the $2Q$ and the $3Q$ state can be clearly distinguished if different rotational domains are imaged or if the tip magnetization is rotated by an external magnetic field.

In contrast, the SP-STM images of the distorted $3Q$ state are very similar to those of the ideal $3Q$ state and much harder to distinguish experimentally. However, the perfect $3Q$ state exhibits only a very weak coupling to the atomic lattice and the energetically preferred rotation of the $3Q$ state is in contrast to SP-STM experiments for hcp-Mn/Re(0001) [6]. The reduced symmetry of the distorted $3Q$ state, however, facilitates an effective coupling to the atomic lattice, e.g., via the easy in-plane magnetic anisotropy of hcp-Mn/Re(0001).

In conclusion, we have demonstrated that topological-chiral magnetic interactions can be significant in ultrathin films. Their competition with biquadratic and four-spin interactions can lead to unexpected types of magnetic ground states such as the $2Q$ or the distorted $3Q$ state. The experimental verification of these spin structures would provide direct evidence of the topological-chiral magnetic interactions.

We gratefully acknowledge computing time at the supercomputer of the North-German Supercomputing Alliance (HLRN) and financial support from the Deutsche Forschungsgemeinschaft (DFG) via Projects No. 418425860 and No. 408119516. It is our pleasure to thank Y. Mokrousov, K. von Bergmann, L. Stühmer-Herrmann, M. Goerzen, M. Gutzeit, and S. Paul for valuable discussions.

[1] A. Fert, N. Reyren, and V. Cros, Magnetic skyrmions: advances in physics and potential applications, Nat. Rev. Mater. **2**, 17031 (2017).

[2] J. Grollier, D. Querlioz, K. Camsari, and M. D. Stiles, Neuromorphic spintronics, Nat. Electron. **3**, 360 (2020).

[3] M. Bode, M. Heide, K. von Bergmann, P. Ferriani, S. Heinze, G. Bihlmayer, A. Kubetzka, O. Pietzsch, S. Blügel, and R. Wiesendanger, Chiral magnetic order at surfaces driven by inversion asymmetry, Nature (London) **447**, 190 (2007).

[4] P. Kurz, G. Bihlmayer, K. Hirai, and S. Blügel, Three-Dimensional Spin Structure on a Two-Dimensional Lattice: Mn/Cu(111), Phys. Rev. Lett. **86**, 1106 (2001).

[5] S. Hayami, R. Ozawa, and Y. Motome, Effective bilinear-biquadratic model for noncoplanar ordering in itinerant magnets, Phys. Rev. B **95**, 224424 (2017).

[6] J. Spethmann, S. Meyer, K. von Bergmann, R. Wiesendanger, S. Heinze, and A. Kubetzka, Discovery of Magnetic Single- and Triple-**q** States in Mn/Re(0001), Phys. Rev. Lett. **124**, 227203 (2020).

[7] S. Heinze, K. von Bergmann, M. Menzel, J. Brede, A. Kubetzka, R. Wiesendanger, G. Bihlmayer, and S. Blügel, Spontaneous atomic-scale magnetic skyrmion lattice in two dimensions, Nat. Phys. **7**, 713 (2011).

[8] M. Hoffmann, J. Weischenberg, B. Dupé, F. Freimuth, P. Ferriani, Y. Mokrousov, and S. Heinze, Topological orbital magnetization and emergent Hall effect of an atomic-scale spin lattice at a surface, Phys. Rev. B **92**, 020401(R) (2015).

[9] K. von Bergmann, M. Menzel, A. Kubetzka, and R. Wiesendanger, Influence of the local atom configuration on a hexagonal skyrmion lattice, Nano Lett. **15**, 3280 (2015).

[10] M. Takahashi, Half-filled Hubbard model at low temperature, J. Phys. C: Solid State Phys. **10**, 1289 (1977).

[11] A. H. MacDonald, S. M. Girvin, and D. Yoshioka, $\frac{t}{U}$ expansion for the Hubbard model, Phys. Rev. B **37**, 9753 (1988).

[12] M. Hoffmann and S. Blügel, Systematic derivation of realistic spin models for beyond-Heisenberg solids, Phys. Rev. B **101**, 024418 (2020).

[13] S. Grytsiuk, J.-P. Hanke, M. Hoffmann, J. Bouaziz, O. Gomonay, G. Bihlmayer, S. Lounis, Y. Mokrousov, and S. Blügel, Topological-chiral magnetic interactions driven by emergent orbital magnetism, Nat. Commun. **11**, 511 (2020).

[14] A. Lászlóffy, L. Rózsa, K. Palotás, L. Udvardi, and L. Szunyogh, Magnetic structure of monatomic Fe chains on Re(0001): Emergence of chiral multispin interactions, Phys. Rev. B **99**, 184430 (2019).

[15] S. Brinker, M. dos Santos Dias, and S. Lounis, The chiral biquadratic pair interaction, New J. Phys. **21**, 083015 (2019).

[16] S. Mankovsky, S. Polesya, and H. Ebert, Extension of the standard heisenberg hamiltonian to multispin exchange interactions, Phys. Rev. B **101**, 174401 (2020).

[17] J.-P. Hanke, F. Freimuth, A. K. Nandy, H. Zhang, S. Blügel, and Y. Mokrousov, Role of Berry phase theory for describing orbital magnetism: From magnetic heterostructures to topological orbital ferromagnets, Phys. Rev. B **94**, 121114(R) (2016).

[18] J. Bedow, E. Mascot, T. Posske, G. S. Uhrig, R. Wiesendanger, S. Rachel, and D. K. Morr, Topological superconductivity induced by a triple-q magnetic structure, Phys. Rev. B **102**, 180504(R) (2020).

[19] See https://www.flapw.de.

[20] M. Weinert, G. Schneider, R. Podloucky, and J. Redinger, FLAPW: applications and implementations, J. Phys.: Condens. Matter **21**, 084201 (2009).

[21] P. Kurz, F. Förster, L. Nordström, G. Bihlmayer, and S. Blügel, *Ab initio* treatment of noncollinear magnets with the full-potential linearized augmented plane wave method, Phys. Rev. B **69**, 024415 (2004).

[22] See https://www.vasp.at.

[23] G. Kresse and J. Furthmüller, Efficient iterative schemes for *ab initio* total-energy calculations using a plane-wave basis set, Phys. Rev. B **54**, 11169 (1996).

[24] P. E. Blöchl, Projector augmented-wave method, Phys. Rev. B **50**, 17953 (1994).

[25] G. Kresse and D. Joubert, From ultrasoft pseudopotentials to the projector augmented-wave method, Phys. Rev. B **59**, 1758 (1999).

[26] See Supplemental Material at http://link.aps.org/supplemental/10.1103/PhysRevB.104.L180404 for computational details and derivation of fitting functions.

[27] D.-P. Ji, Q. Zhu, and S.-Q. Wang, Detailed first-principles studies on surface energy and work function of hexagonal metals, Surf. Sci. **651**, 137 (2016).

[28] W. Li, S. Paul, K. von Bergmann, S. Heinze, and R. Wiesendanger, Stacking-Dependent Spin Interactions in Pd/Fe Bilayers on Re(0001), Phys. Rev. Lett. **125**, 227205 (2020).

[29] Note that there is another topological-chiral magnetic interaction, the spin-chiral interaction [13], which vanishes in the absence of spin-orbit coupling.

[30] P. Ferriani, I. Turek, S. Heinze, G. Bihlmayer, and S. Blügel, Magnetic Phase Control in Monolayer Films by Substrate Tuning, Phys. Rev. Lett. **99**, 187203 (2007).

[31] N. M. Rosengaard and B. Johansson, Finite-temperature study of itinerant ferromagnetism in Fe, Co, and Ni, Phys. Rev. B **55**, 14975 (1997).

[32] A. I. Liechtenstein, M. I. Katsnelson, V. P. Antropov, and V. A. Gubanov, Local spin density functional approach to the theory of exchange interactions in ferromagnetic metals and alloys, J. Magn. Magn. Mater. **67**, 65 (1987).

[33] In the VASP calculation the 2Q state is by 0.07 meV/Mn atom lower than the distorted 3Q state and in the FLEUR calculation by 0.5 meV/Mn atom.

[34] S. Heinze, Simulation of spin-polarized scanning tunneling microscopy images of nanoscale non-collinear magnetic structures, Appl. Phys. A **85**, 407 (2006).

[35] D. Wortmann, S. Heinze, P. Kurz, G. Bihlmayer, and S. Blügel, Resolving Complex Atomic-Scale Spin Structures by Spin-Polarized Scanning Tunneling Microscopy, Phys. Rev. Lett. **86**, 4132 (2001).

[36] K. von Bergmann, A. Kubetzka, O. Pietzsch, and R. Wiesendanger, Interface-induced chiral domain walls, spin spirals and skyrmions revealed by spin-polarized scanning tunneling microscopy, J. Phys.: Condens. Matter **26**, 394002 (2014).